

# Prediction of the Most Fire-Sensitive Point in Building Structures with Differentiable Agents for Thermal Simulators

Yuan Xinjie

Pacific Earthquake Engineering Research (PEER) Center  
University of California, Berkeley  
Berkeley, California, U.S.A &  
Shenzhen International Graduate School  
Tsinghua University  
Shenzhen, Guangdong, China  
yuan.xinjie@berkeley.edu

Khalid M. Mosalam\*

Pacific Earthquake Engineering Research (PEER) Center  
University of California, Berkeley &  
Department of Civil and Environmental Engineering  
University of California, Berkeley  
Berkeley, California, U.S.A  
mosalam@berkeley.edu

**Abstract**—Fire safety is a critical area of research in civil and mechanical engineering, particularly in ensuring the structural stability of buildings during fire events. The Most Fire-Sensitive Point (MFSP) in a structure is the location where a fire would cause the greatest impact on structural stability. Accurate prediction of the MFSP is vital for streamlining structural assessments and optimizing the design process. This paper presents a novel framework for MFSP prediction using a neural network-based approach that integrates fire dynamics and finite element analysis through a differentiable agent model. The framework focuses on predicting the Maximum Interstory Drift Ratio (MIDR), a key indicator of structural performance under fire conditions. By leveraging the differentiable agent model, we efficiently generate labeled data for MFSP and directly train a predictor for this critical metric. To achieve this, we generated extensive simulation data encompassing structural and fire scenarios and employed graph neural networks to represent the building structures. Transfer learning was applied to optimize the training process, and an edge update mechanism was introduced to dynamically adjust edge attributes, reflecting property changes under fire conditions. The proposed model was rigorously evaluated on simulation data, demonstrating strong performance in accurately predicting both MIDR and MFSP, thus advancing fire safety analysis for building structures.

**Index Terms**—Differentiable Agents, Finite Element Analysis, Fire Dynamics, Graph Neural Networks, Most Fire-Sensitive Point, Structural stability, Thermal Simulation.

## I. INTRODUCTION

With the rapid urbanization and increasing complexity of building structures, fire safety has become a critical global issue. Fires pose significant challenges to structural integrity and stability of buildings, making it essential to incorporate fire safety measures during the design phase to enhance resilience and prevent catastrophic failures. The devastating impact of recent wildfires in California highlights the urgency

of improving fire risk assessment and mitigation measures in the built environment [3].

A standard fire safety requirement mandates that a building must withstand collapse for at least one hour under fire conditions at any specific point within the structure. Current methods to ensure this involve computational simulations, where fire scenarios are simulated at all potential locations within the building structure. This exhaustive approach is computationally expensive and time-consuming, increasing the cost and duration of structural design.

To address this inefficiency, we propose a novel method neural network-based framework to predict the Most Fire-Sensitive Point (MFSP) –the location where fire has the greatest impact on a structure’s stability. By identifying the MFSP, designers need to simulate only a single fire scenario to evaluate structural compliance, significantly reducing computational costs and enhancing design efficiency.

Training an MFSP predictor using traditional supervised learning is impractical due to the lack of labeled data. Generating such data requires simulating fire dynamics at every possible location within a structure –a process that is both labor-intensive and computationally prohibitive. To overcome this, we introduce an innovative framework comprising two neural network predictors: the Maximum Interstory Drift Ratio (MIDR) Predictor and the MFSP Predictor.

The workflow begins with Finite Element Analysis (FEA) simulations for a limited set of fire scenarios, which are used to train the MIDR Predictor. This predictor serves as a highly efficient and *differentiable agent*, simulating structural responses under fire conditions. The differentiable agent is then used in two ways: (1) as an indicator to directly train the MFSP predictor to be an “argmaxer” of the agent, and (2) to generate synthetic data to assist in the training, enabling it to efficiently identify the MFSP without extensive real-world data.

The primary contributions of this research are as follows:

Professor Khalid M. Mosalam is the corresponding author.

This paper is currently under review at *Computer-Aided Civil and Infrastructure Engineering*.

- **Data Creation:** We generated a large dataset of 33,000 building structures, encompassing their geometry, material properties, and nodal displacements under gravity loads. A subset of 1,573 structures was further subjected to fire scenario simulations, including nodal displacements obtained using OpenSees [21].
- **Prediction Framework:** We propose a novel framework combining a differentiable agent for fire dynamics and FEA simulation with an MFSP predictor to identify the most fire-sensitive point.
- **Graph Neural Networks (GNNs):** We employ GNNs to model building structures and utilize Transfer Learning (TL) for efficient training. An Edge Update (EU) mechanism is introduced to account for changes in structural properties under fire scenarios.
- **Open-Source Resources:** We provide the dataset and implementation details via a public GitHub repository: [https://github.com/STAIRlab/MFSP\\_Prediction](https://github.com/STAIRlab/MFSP_Prediction).

The remainder of this paper is organized as follows: Section II reviews relevant literature on fire dynamics, building structure interactions, and fire simulation tools. Section III provides an overview of the proposed system architecture. Sections IV, V, and VI detail dataset generation, the MIDR predictor, and the MSFP predictor, respectively. Implementation details and evaluation results are presented in Section VII. Finally, concluding remarks including future research directions are discussed in Section VIII. Through this research, we aim to enhance fire risk assessment accuracy and efficiency, providing a robust tool to support the design of safer, more resilient building structures.

## II. LITERATURE REVIEW

Understanding the interaction between fire dynamics and building structures is fundamental to designing safer, more resilient systems. Resilience, in this context, encompasses robustness, adaptability, recoverability, and redundancy, ensuring systems can withstand, adapt to, and recover from adverse events. Recent advances in FEA, Machine Learning (ML), and physics-informed simulations have provided powerful tools for analyzing and predicting structural performance under fire conditions. This section reviews key contributions in these domains, identifies gaps, and motivates the integration of differentiable agents with thermal simulators for enhanced fire analysis in buildings.

### A. Fire Dynamics in Buildings

The interplay between thermal loads and structural integrity during fire events has been extensively studied. Early work in [1] introduced a method for simulating heat transfer in steel structures. This approach was later enhanced to incorporate transient thermal responses and load redistribution effects [17], which remain vital for predicting collapse mechanisms under high-temperature conditions [10]. Despite these advances, traditional simulations often face challenges with scalability and computational efficiency in large-scale structures.

### B. Advancements in Thermal Simulation

Thermal simulation tools have evolved significantly, with recent advancements focusing on computational efficiency and accuracy. Differentiable simulators, in particular, represent a transformative paradigm by enabling gradient-based optimization for thermal and structural problems [2]. These simulators are increasingly applied in various fields, including the modeling of thermal conduction in complex structures and the optimization of structural materials for thermal resistance under uncertain environmental loads. For example, simulation tool like the Fire Dynamic Simulator (FDS) have been extensively utilized in fire engineering to model thermal and structural interactions with high fidelity [19]. Furthermore, emerging differentiable simulation frameworks, such as Taichi, provide a robust foundation for high-performance computations, enabling efficient optimization in physical modeling and material design [13]. These frameworks represent a critical leap in bridging the gap between simulation accuracy and computational efficiency.

### C. ML in Structural Analysis

Recent advancements in ML have significantly impacted structural engineering, particularly in predicting building responses under fire scenarios. For example, [23] employed modular Long Short-Term Memory (LSTM) networks to accurately predict building displacements during fire events, showcasing the potential of sequential models in time-dependent structural analysis. Similarly, GNNs, known for their strong ability to model spatially structured data [16], have gained traction in civil engineering [15]. Notably, [5] applied GNNs to predict structural responses under gravity loads, further demonstrating their efficacy in representing complex structural relationships. These developments highlight the growing role of ML techniques in enhancing the efficiency and accuracy of structural response predictions, particularly under challenging conditions like fire and other extreme events.

### D. Critical Gaps and Opportunities

Despite significant advancements, key challenges persist in structural analysis. Traditional FEA methods remain computationally intensive, limiting their scalability for large-scale simulations. Additionally, the application of GNNs in structural analysis is still in its early stages. While GNNs have been successfully employed for structural response prediction, their application to fire scenarios remains unexplored. Furthermore, GNNs have yet to fully harness global structural knowledge to identify the most vulnerable components within a structure.

A promising solution lies in treating the neural network models as differentiable agents and integrating them with thermal simulators. This approach combines the computational efficiency of ML with the physical accuracy of simulation-based methods. Expanding the use of GNNs to predict fire-sensitive points in structures could significantly improve early failure detection. Such advancements have the potential to revolutionize fire safety engineering and structural design, enhancing both resilience and efficiency.

### III. SYSTEM OVERVIEW

The primary goal of this work is to accurately predict the MFSP in a building structure subjected to various fire scenarios. To achieve this, we propose an integrated framework that combines GNNs and FEA. The system architecture is illustrated in Figure 1 and comprises two key components: the Maximum Interstory Drift Ratio (MIDR) Predictor and the MFSP Predictor. This framework seamlessly integrates physics-based simulations, GNN-driven predictive modeling, and data-driven techniques, enabling efficient and accurate MFSP prediction, providing a powerful tool for proactive fire safety analysis and risk mitigation in building structures.

#### A. MIDR Predictor

The MIDR Predictor is a GNN-based model designed to estimate the MIDR of a building under a given fire scenario. The inputs to this model include:

- 1) **Structural configuration:** Building geometry, material property, and gravity loads.
- 2) **Fire Location:** The specific point where the fire is initiated within the building.

A GNN processes this input to represent the structural configuration and fire location as a graph. The MIDR Predictor is trained on labeled data generated using OpenSees, a robust open-source FEA framework [21]. These labels represent detailed structural responses under various fire conditions. Once trained, the MIDR Predictor functions as a differentiable agent, offering computationally efficient MIDR estimates. Its capabilities include:

- **Annotating Datasets:** Assigning MIDR values to support subsequent analyses.
- **Integrating with Neural Networks:** Reducing the computational cost typically associated with simulation-based methods.

#### B. MFSP Predictor

The MFSP Predictor acts as an “argmaxer module” for the MIDR Predictor, identifying the fire location that results in the highest MIDR. This location, deemed the MFSP, corresponds to the point of greatest structural vulnerability. By leveraging the structural graph as input and utilizing the MIDR Predictor’s outputs, the MFSP Predictor efficiently pinpoints the critical fire location.

#### C. Data Generation and Training Pipeline

To ensure robustness and generalizability, we introduce a comprehensive data generator pipeline:

- 1) **Building Data Generator:** This component creates synthetic datasets for diverse building configurations, including geometry, material, and gravity loads.
- 2) **FEA Simulations:** With the high-fidelity FEA simulation software, OpenSees, the gravity simulation is first conducted to confirm the rationality of the synthetic dataset. Further, a subset of the generated configurations undergoes fire scenario simulations using OpenSees

based on a rule-based thermal load generation method. These simulations produce **labeled data** detailing structural responses to various fire locations, forming training and testing sets for the MIDR Predictor.

- 3) **Unlabeled Data Utilization:** The remaining configurations, without MIDR labels from FEA simulation, are used to train and test the MFSP Predictor, leveraging the MIDR Predictor as a computationally efficient, yet accurate, *surrogate* model. Although the unlabeled data does not undergo FEA simulation, they can be rapidly *pseudo labeled* by this surrogate model.

### IV. DATASET GENERATION

To train the proposed neural network, we constructed a dataset comprising building structure data and a subset of fire scenario data. The dataset generation process is illustrated in Figure 2. A total of 33,000 building structures with geometric details, material properties, and gravity loads were initially created. Out of these, 3,000 structures were selected as labeled data, and the remaining 30,000 were designated as unlabeled data. Further, about half of them filtered out due to instability under gravity loads only. This section details the step-by-step process for generating the dataset, including geometry creation, material property assignment, and simulations due to gravity loads and fire scenarios.

#### A. Geometry Generation

The geometry of the building structures forms the foundation of the dataset. Regular three-dimensional (3D) structural configurations resembling parking structures or shopping malls are generated, with parameters such as building floor dimensions and story heights selected randomly. Each building structure is composed of multiple rooms, which serve as the basic unit in this study. A room herein is a cubic space defined by a specific length, width, and height. Within a structure, rooms of the same dimensions are uniformly arranged along the length, width, and height, corresponding to the  $x$ -,  $y$ -, and  $z$ -axes, respectively. Structures vary in room size and number of rooms along each axis. Specifically, the length, width, and height of each room are independently sampled from a uniform distribution within the interval [2, 5] meters along the 3 directions of the structure. Similarly, the number of rooms along each axis is uniformly sampled as an integer from 2 to 7, independently. This also implies that the maximum number of stories of the buildings simulated in this study is 7.

To introduce variability and simulate real-world scenarios, approximately 8% of structural elements (beams or columns) are randomly removed after initial geometry creation. However, this removal does not affect the definition of rooms in the structure. This adjustment reflects functional diversity often observed in real buildings, such as open spaces designed for activities in shopping malls. Examples of the generated geometries are illustrated in Figure 3, showcasing the diversity and realism of the dataset. Several studies, e.g., [18], [22], determined the statistical properties of different geometrical and

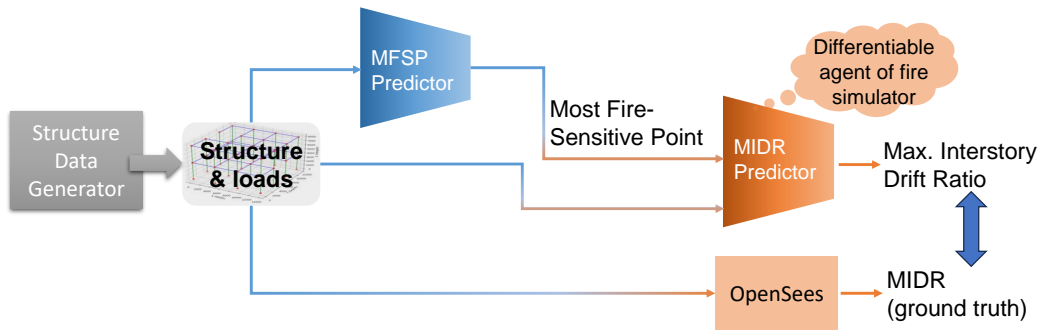


Fig. 1: Overview of the proposed framework for predicting the MFSP in building structures.

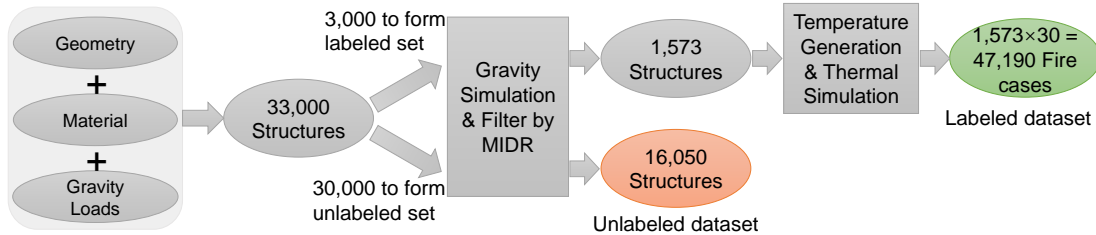


Fig. 2: Workflow for dataset generation (geometry, material property, gravity loads, and fire scenarios).

material properties of building structures. From these studies a range of the coefficient of variations of the corresponding variables to these properties was identified as 3.3% to 17.5%. The chosen 8% is selected within this range.

### B. Material Properties

Steel is chosen as the primary material for the structures. To reflect real-world variations, we randomly assign one of five slightly different steel material types to each structural element. These variations simulate differences arising from manufacturing batches or regional material properties. The range of material properties is provided in Table I.

TABLE I: Material properties ranges for steel structures.

Property	Range
Young's modulus	[168, 252] GPa
Yield strength	[220, 330] MPa
Strain-hardening ratio	[0.8, 1.2] %

### C. Gravity Loads

Gravity loads are applied to columns and beams based on their position and function. For columns, only self-weight is considered, while beams support additional loads from reinforced concrete slabs, people as live load, and building content. Edge beams, which support only one side, carry less load than interior beams. The ranges of gravity loads are listed in Table II. Structures that failed to meet a MIDR threshold of 1% under gravity loads were deemed unstable and filtered out,

as such configurations of randomly chosen geometry, material, and gravity load combinations were considered unrealistic from a regulatory and practicality points of view.

TABLE II: Gravity load ranges for beams and columns.

Element	Range (kN/m)
Column	[0.5, 1.0]
Edge Beam	[1.5, 4.5]
Interior Beam	[3.0, 7.5]

### D. Rule-based Thermal Load Generation

To evaluate a building's structural response during a fire, we employed a simplified rule-based approach to thermal load generation. Previous studies [23] have demonstrated that steel structures rapidly equilibrate with surrounding gases temperatures due to efficient heat exchange. Consequently, gas temperatures can be directly used as inputs for FEA tools, e.g., OpenSees, simplifying the process of modeling thermal loads.

Accurately simulating temperature fields in fire scenarios poses significant challenges. Advanced thermodynamic simulations, such as those performed using Fire Dynamics Simulator (FDS) [20], provide precise temperature predictions. However, these methods are hindered by high computational costs, prolonging execution times, and limited scalability, making them impractical for generating large datasets. Additionally, real-world fire loads often display substantial spatial variability across different rooms [7], resulting in scenario-specific temperature fields with limited generalizability. For

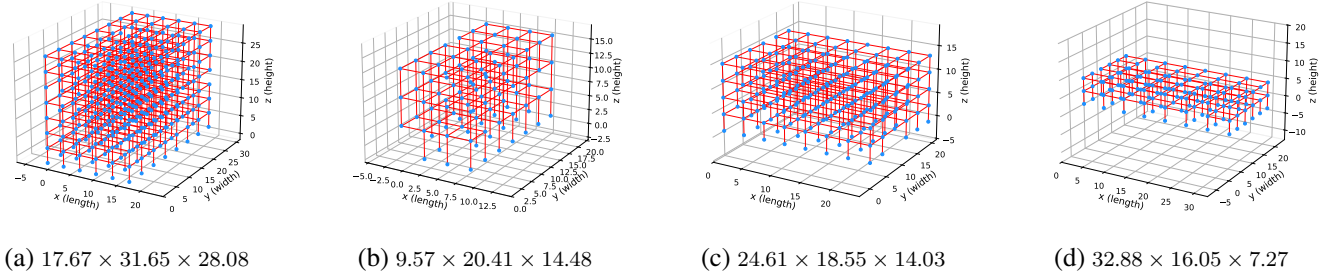


Fig. 3: Examples of generated structural geometry of different sizes (all dimensions in meters).

example, studies on bridge fires [11] have demonstrated that environmental factors, such as wind speeds, can significantly influence temperature distributions. Furthermore, even within identical scenarios, variations in fire modeling methodologies can produce distinctly different temperature fields [6], [27]. These challenges emphasize the need for efficient and adaptable methods to generate fire temperature data.

To address these issues, we adopted a rule-based approach to model temperature variations. According to [25], a typical fire development follows a predictable pattern: during the *growth stage*, the temperature rises slowly and approximately linearly after ignition. This is followed by the *flashover stage*, where temperatures increase rapidly to peak values. After reaching the peak, the temperature either stabilizes or continues to rise slowly until the *decay stage* begins. Inspired by this fire development pattern, we describe the temperature evolution prior to decay in two distinct stages:

- 1) **Initial Linear Increase Stage:** For  $t \in [0, t_1]$ , temperature increases gradually and linearly as the fire spreads through the building. This stage represents the time before the fire directly affects a structural element.
- 2) **ISO 834 Fire Curve Stage:** For  $t \in [t_1, t_{th}]$ , temperature rises rapidly following the ISO 834 curve [14], modeling the direct impact of the fire on the structural element.

The slope of the linear temperature increase,  $c$ , and the transition time,  $t_1$ , are influenced by the spatial relationship between the fire source and the structural element. For the second stage of temperature evolution, we utilize the ISO 834 curve, a widely accepted standard for fire resistance testing. This standardized fire curve describes the temperature rise over time, enabling rapid and consistent thermal fields across various scenarios. Additionally, the duration of fire simulation in this study is set to  $t_{th} = 60$  minutes. This value represents the upper time limit for the temperature evolution of each structural element, providing a consistent basis for analyzing structural responses to fire.

Let  $(x, y, z)$  represents the midpoint of a structural element and  $(x_f, y_f, z_f)$  the fire origin point. Heights  $h$  and  $h_f$  correspond to the respective floor levels of the element and the fire source. The temperature evolution for each element is expressed as:

- 1) Linear Increase Stage ( $0 < t < t_1$ ):

$$T(t) = c \cdot t, \quad (1)$$

where  $c$ , the rate of temperature increase ( $^{\circ}\text{C}/\text{min}$ ), depends on the height difference between the element,  $h$ , and the fire source,  $h_f$ :

$$c = \begin{cases} 5/(h - h_f + 1), & h \geq h_f, \\ 2/(h_f - h), & h < h_f. \end{cases} \quad (2)$$

- 2) ISO 834 Stage ( $t \geq t_1$ ):

$$T(t) = c \cdot t_1 + 345 \log_{10}(8(t - t_1) + 1). \quad (3)$$

The transition (arrival) time  $t_1$ , marking the end of the linear stage, depends on the spatial distance between the fire source and the element. We define the following two Euclidean distances  $L_p$  in the  $xy$  plane and  $L_s$  in the  $xyz$  space:

$$L_p \triangleq \sqrt{(x - x_f)^2 + (y - y_f)^2}, \quad (4)$$

$$L_s \triangleq \sqrt{(x - x_f)^2 + (y - y_f)^2 + (z - z_f)^2}. \quad (5)$$

Accordingly, the transition time,  $t_1$ , is expressed as follows:

$$t_1 = \begin{cases} \beta_1 \cdot (1 - \exp\{-L_s/\alpha_1\}), & h > h_f, \\ \beta_2 \cdot (1 - \exp\{-L_p/\alpha_2\}), & h = h_f, \\ \beta_3 \cdot (1 - \exp\{-L_s/\alpha_3\}), & h < h_f. \end{cases} \quad (6)$$

The parameters  $\beta$  and  $\alpha$  for determining  $t_1$  are summarized in Table III. In this study, we take  $r_{up} = 0.95$  and  $r_{down} = 0.97$ .

TABLE III: Fire spread parameters for  $t_1$  calculations.

Case	$\beta_i$	$\alpha_i$
$i = 1$ , Upward Spread	$16 \left(1 - r_{up}^{ h-h_f }\right) / (1 - r_{up})$	10
$i = 2$ , Horizontal Spread	18	18
$i = 3$ , Downward Spread	$30 \left(1 - r_{down}^{ h-h_f }\right) / (1 - r_{down})$	5

Figure 4 illustrates the  $t_1$  curves for various fire scenarios: fire originating on the lower floor,  $h - h_f = 1$  with rapid upward spread, fire on the same floor,  $h = h_f$  with the fastest spread, and fire on the upper floor,  $h_f - h = 1$  with slower downward propagation. The exponential decay observed in  $t_1$  reflects the accelerating fire propagation speed as the distance increases. Figure 4 also indicates that the employed simplified

model is consistent with the Markov chain-based dynamic model given by [4], where the rooms at the same floor of the fire point start flashover slightly before the corresponding upper floors. Additionally,  $\beta_1$  and  $\beta_3$  are the summation of a geometric sequence, where story level  $h$  is the index. The common ratios  $r_{\text{up}} < 1$  in  $\beta_1$  and  $r_{\text{down}} < 1$  in  $\beta_3$  indicate that the fire speeds up to spread through the next story, which is consistent with the real-world fire spread mechanism given in [12]. The temperature profile within the range  $t \in [0, t_{\text{th}}]$  is subsequently used as the thermal load in OpenSeesRT simulations to compute displacements at each structural node at time  $t_{\text{th}}$ .

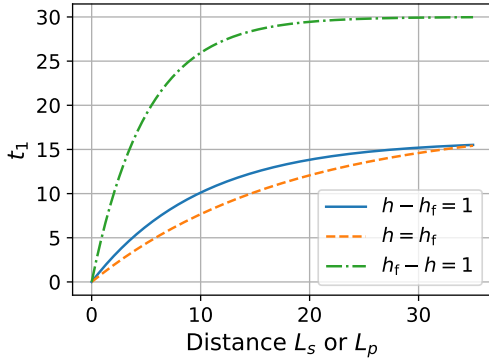


Fig. 4: Three examples for the  $t_1$  curve.

In conclusion, this rule-based approach is a computationally efficient method to approximate fire temperature fields, enabling large-scale dataset generation to train predictive models. By combining ISO 834 fire curves with spatial considerations, the method balances accuracy and scalability, making it a practical solution for thermal load modeling in fire scenarios.

#### E. Interstory Drift Ratio

The Interstory drift ratio (IDR) quantifies the relative displacement between two consecutive floors (interstory displacement) as a percentage of the floor height. It serves as a critical parameter for evaluating structural deformation under external forces, such as seismic or thermal loads. In the context of fire-induced deformation, the IDR provides valuable insight into the relative movement between floors as a structure experiences thermal expansion or contraction. Mathematically, the IDR for a given node  $i$ , i.e.,  $d_i$ , is defined as follows:

$$d_i = \sqrt{(\Delta x_i)^2 + (\Delta y_i)^2} / H \times 100 \%, \quad (7)$$

where the numerator represents the relative displacement (in the horizontal plane  $xy$ ) of node  $i$  with respect to the corresponding node on the floor below, and  $H$  denotes the story height between these two floors. The IDR is a crucial metric for assessing the structural integrity under extreme conditions. Excessively high drift ratios can indicate significant structural deformation, potentially leading to damage or collapse. For this study, the IDR at  $t_{\text{th}}$  is computed using displacement data

obtained from OpenSees simulations under thermal loading during fire scenarios.

#### F. OpenSees Simulation

The thermal and mechanical responses of 3D frame structures under combined fire and gravity loads are simulated using OpenSees [21], specifically OpenSeesRT [24]. Each structural model features six degrees of freedom per node, with linear geometric transformations (`geomTransf: Linear`) defining element orientations. Material behavior is temperature-dependent and modeled with `Steel01Thermal`, while fiber-based sections (`FiberThermal`) capture nonlinear interactions between thermal and mechanical responses at the cross-section level. Structural elements are represented as displacement-based beam-column elements (`dispBeamColumnThermal`), accounting for both thermal and mechanical load effects.

The analysis begins with the application of gravity loads to establish equilibrium, followed by incremental thermal loads simulating fire exposure. A static nonlinear solver using the `ExpressNewton` algorithm ensures efficient convergence, while the `NormDispIncr` test maintains accuracy. An incremental `LoadControl` scheme with small step sizes is employed to guarantee numerical stability, using 10% for gravity loads and 1% for thermal loads. In the thermal load analysis of steel structures using OpenSeesRT, the material properties (e.g., Young's modulus and yield strength) are adjusted at increasing temperatures according to [8], particularly its Table 3.1: Reduction factors for the stress-strain relationship of carbon steel at elevated temperatures. OpenSees documentation [9] provides several examples of thermal analysis for different steel materials.

This modeling framework accommodates variations in material properties, cross-sectional geometries, and temperature profiles, providing robust simulations of structural behavior under fire conditions. The primary settings and configurations for the OpenSeesRT simulations are summarized in Table IV.

TABLE IV: Key settings of OpenSeesRT simulation scripts.

Modeling Aspect	Details
Geometry Transformation	3D models; 6 degrees of freedom per node <code>geomTransf: Linear</code>
Material Section	<code>Steel01Thermal</code> <code>FiberThermal</code> ; Cross-section dimensions: 0.1 m $\times$ 0.1 m
Element type Loading	<code>dispBeamColumnThermal</code> Gravity loads: <code>beamUniform</code> ; Thermal loads: <code>beamThermal</code>
Integration scheme	Incremental <code>LoadControl</code> ; Step size: 10% (gravity analysis), 1% (thermal analysis)
Nonlinear solver	<code>ExpressNewton</code> algorithm; <code>UmfPack</code> solver; Convergence test: <code>NormDispIncr</code> tolerance: $10^{-8}$ ; Maximum # iterations per step: 1000.

For each structure in the labeled dataset, 30 fire points are selected using a dual-granularity approach to ensure they are well-distributed. Specifically, rooms are sequentially selected,

with one fire point randomly chosen within each selected room. If a building is large and contains more than 30 rooms, we randomly select 30 rooms without replacement, i.e., ensuring that no more than one fire point is located in the same room. Conversely, if the building is small and has fewer than 30 rooms, all rooms are initially selected, with one fire point randomly assigned to each room. Additionally, rooms are then selected with replacement until a total of 30 fire points are assigned. This selection method prevents fire points from clustering too closely while maintaining an element of randomness. By distributing fire points in this manner, the 30 fire scenarios are effectively utilized, enabling a more comprehensive characterizing of how the structures respond under fire conditions.

### G. Summary of the Dataset Generation

As discussed in this section and related to Figure 2, three key steps were considered in the development of the dataset:

- 1) **Filtering Process:** Structures with MIDR exceeding 1% under gravity loads were excluded, resulting in 1,573 labeled structures retained for fire simulation and 16,050 unlabeled structures for training the MFSP Predictor.
- 2) **Fire Simulations:** For each retained labeled structure, 30 fire scenarios were simulated using OpenSeesRT, yielding 47,190 fire cases.
- 3) **Data Distribution Check:** MIDR distributions for labeled and unlabeled data under gravity loads were highly similar, because both datasets were generated using the same method. Under fire conditions, the MIDR distribution shifted, reflecting significant structural deformation with values reaching a maximum of about 6%, an average of 1.70%, and a standard deviation of 1.12%. This step ensured a diverse and comprehensive dataset for the predictive framework.

The statistical distribution histograms for MIDR (after applying the 1% filtering threshold) under different loading conditions are plotted in Figure 5 to illustrate the data characteristics. Figures 5(a) and 5(b) show the MIDR distributions of the labeled and unlabeled data, respectively, under gravitational loads only. Figure 5(c) depicts the MIDR distribution of the labeled data under the combined effects of gravity and fire loads. Under fire loading, the structures exhibit significant deformation, leading to a noticeably right-shifted MIDR distribution.

## V. MAXIMUM INTERSTORY DRIFT RATIO PREDICTOR

The MIDR Predictor functions as a differentiable agent for the FEA simulators. It accepts building structure data and fire coordinates as inputs and predicts the MIDR of the building under fire exposure. Leveraging GNNs for structural representation, the predictor integrates Transfer Learning (TL) to optimize data utilization while focusing on MIDR prediction. Additionally, an innovative Edge Update (EU) module, to update the edge attributes of the GNNs, is introduced to capture changes in element attributes during fire scenarios.

### A. Graph Neural Networks

1) *Overview of GNNs:* Building structures and graphs share an intrinsic similarity: structural nodes correspond to graph nodes, and structural elements (e.g., beams and columns) map naturally to graph edges. This analogy forms the basis for utilizing GNNs in structural data processing.

A typical GNN consists of multiple stacked layers, where the output of one layer serves as the input for the next. Each layer executes three core operations –Message Passing, Aggregation, and Update– which can be expressed as follows:

$$\mathbf{v}_i^k = \gamma^k \left( \mathbf{v}_i^{k-1}, \bigoplus_{j \in \mathcal{N}(i)} \phi^k(\mathbf{v}_i^{k-1}, \mathbf{v}_j^{k-1}, \mathbf{e}_{j,i}) \right), \quad (8)$$

where  $\gamma^k(\cdot)$  and  $\phi^k(\cdot)$  represent the update and message functions, respectively,  $\bigoplus$  is the aggregation operation, e.g., sum, mean, or max,  $\mathcal{N}(i)$  denotes the set of neighboring nodes of node  $i$ , and  $\mathbf{v}_i^k$  and  $\mathbf{e}_{j,i}$  are the attributes of node  $i$  at the  $k$ -th layer and of the edge from node  $j$  to node  $i$ , respectively. Here, both  $\gamma^k(\cdot)$  and  $\phi^k(\cdot)$  are typically chosen as Multi-Layer Perceptrons (MLPs), i.e., fully connected neural networks.

Figure 6 provides a schematic of a GNN with  $K$  layers, illustrating the role of node and edge encoders, as well as the EU mechanism. The shown GNN incorporates initial node and edge encoders to transform input features into higher-dimensional spaces and utilizes an EU mechanism to dynamically update edge attributes during each layer to capture the changes of the elements in the fire scenario.

2) *Handling structural data:* A significant challenge in GNNs is the *over-smoothing*, where during each layer’s update process, a node’s attributes aggregate information from its neighboring nodes. Consequently, increasing the number of layers causes node attributes to homogenize, losing their specificity and negatively impacting the model’s performance. This issue is particularly pronounced in building structures with varying story counts and number of nodes, such as 2-story vs. 7-story buildings. If both are passed through a 7-layer GNN, the node attributes of the 2-story building would experience severe over-smoothing. To mitigate this problem, we adopt the method from [5], restricting the number of GNN layers for each graph, i.e., building structure herein, to the building’s maximum number of stories, ensuring critical information about fire propagation is retained in the node attributes without over-smoothing.

Beams and columns exhibit distinct load characteristics that influence how they are represented in graph-based model of a structure. Beams primarily bear gravity loads that act perpendicular to their axial direction, which aligns with their structural function in resisting bending moments. Under thermal expansion due to fire, these loads affect both end nodes of the beam. As a result, when representing beams in a graph model, it is intuitive to treat them as *undirected edges*, reflecting their bidirectional influence on the connected nodes. Columns, on the other hand, experience gravity loads along their axial direction, typically directed downward, which is consistent with their role in supporting vertical loads. When a column

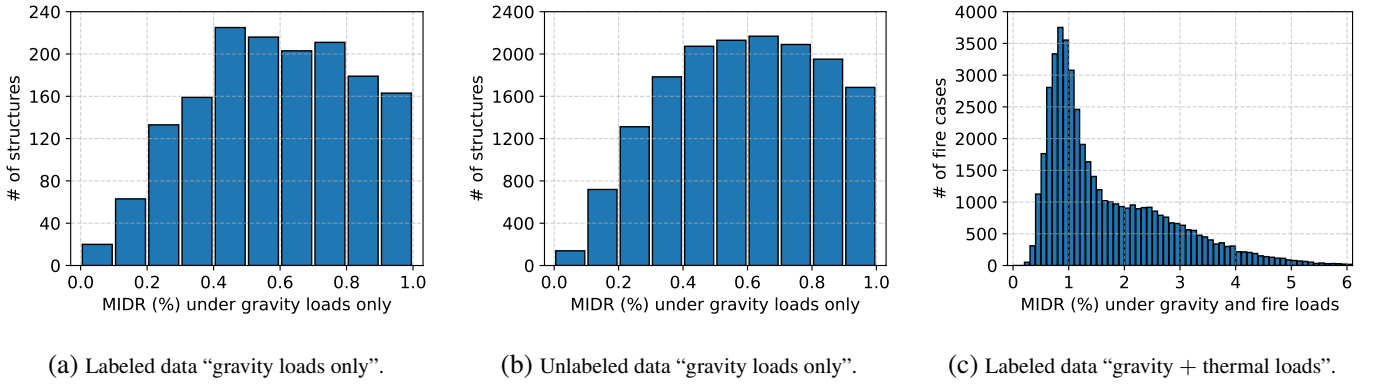


Fig. 5: Histograms of MIDR for labeled and unlabeled structures with gravity loads and fire cases.

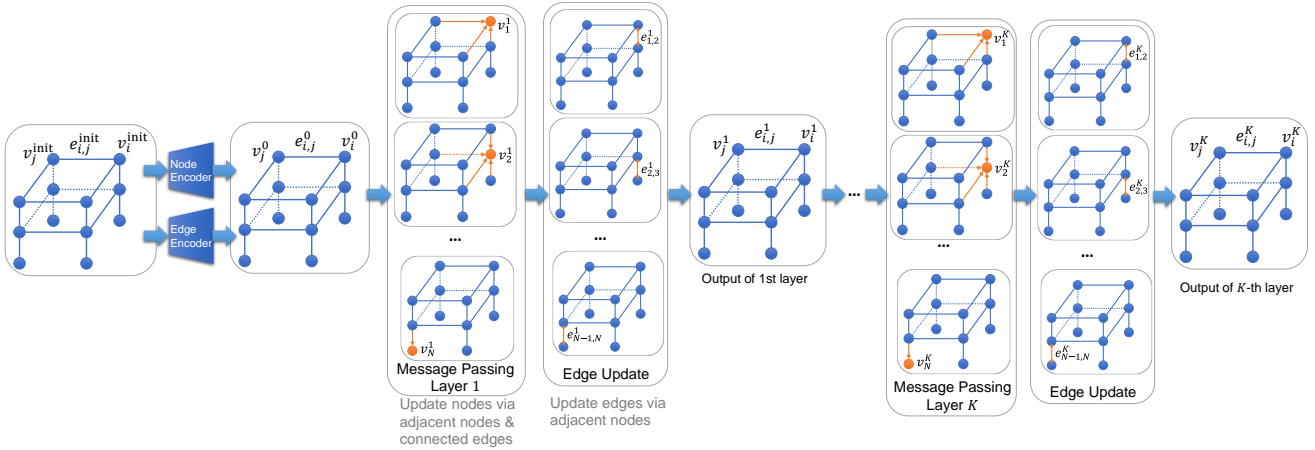


Fig. 6: Illustration of a  $K$ -layer GNN architecture. The figure demonstrates information flow within the network for a graph with  $N$  nodes.

deforms under loads (due to thermal expansion, lateral loads, or gravity), the displacements at any point in the column influence the displacements above it due to load transfer mechanics. Conceptually, this effect continues sequentially upward along the column length. However, in the mathematical formulation of the FEA, the computation involves solving global equations that inherently account for all inter-dependencies between elements and boundary conditions simultaneously, not sequentially. Accordingly, representing columns as *directed edges* might initially seem appropriate, as it allows separate transmission of force and displacement information. However, in GNNs, undirected graphs are commonly implemented by duplicating directed edges and reversing their directions to ensure bidirectional information flow. Given this practical implementation in GNNs, both beams and columns are treated as **undirected edges** in our graph model. This approach simplifies the representation while preserving the necessary information flow for structural analysis.

3) *Input attributes*: In our framework, gravity loads and thermal loads are applied to beams or columns, which dictate the information encapsulated within the nodes and edges of the graph representation.

a) *Node Attributes*:: The information associated with each node  $i$  in the structure includes geometric details, specifically the 3D coordinates  $(x_i, y_i, z_i)$ . These coordinates are essential for representing the spatial configuration of the structure. Additionally, since floor height,  $h_i$ , is a critical factor in fire scenarios, it is also included as a key node attribute. To account for fire location, the coordinates of the fire source  $(x_f, y_f, z_f)$  and its corresponding floor height  $h_f$  are incorporated into the node attributes. To enhance the model’s ability to capture fire-related information, we compute the differences between the node coordinates and its floor height on one hand and the fire location coordinates and its floor height on the other hand, i.e.,  $(x_i - x_f, y_i - y_f, z_i - z_f, h_i - h_f)$ . Additionally, the Euclidean distance between the  $i$ -th node and the fire location is calculated according to Equation (5) with  $x = x_i$ ,  $y = y_i$ , and  $z = z_i$ . These features collectively form the initial attributes of each node  $i$ , denoted as  $v_i^{\text{init}}$ , comprising a total of 13 features.

b) *Edge Attributes*:: The edges between nodes represent the structural elements (beams and columns) and encapsulate the following attributes:



- 1) **Material properties:** Young’s modulus at ambient temperature, yield strength, and strain-hardening ratio.
- 2) **Geometric properties:** Length, floor level, and orientation. Note that the orientation is encoded using a one-hot representation to indicate alignment along the  $x$ -axis,  $y$ -axis, or  $z$ -axis.
- 3) **Gravity loads:** Magnitude of applied load on the element.

The initial attributes of each edge  $(i, j)$ , denoted as  $e_{i,j}^{\text{init}}$ , are represented by 9-dimensional vector combining these three sets of attributes.

*c) Feature Encoding:* The raw node and edge attributes are not directly input into the GNN. Instead, encoders are employed to map the initial attributes into higher-dimensional spaces, which improve the model’s capacity for feature representation:

- **Node encoder:** Extends the 13-dimensional node attributes to  $v_i^0$  with a higher dimensionality, e.g., 64 dimensions. The superscript 0 indicates it is the input of the first GNN layer.
- **Edge encoder:** Maps the 9-dimensional edge attributes to  $e_{i,j}$  with a higher-dimensional representation, e.g., 32 dimensions.

These encoders, implemented as simple single-hidden-layer MLPs, ensures that the feature dimensions across different layers remain consistent. This consistency is crucial because the number of GNN layers a structure passes through is determined by its maximum number of stories, consistent dimensionality allows for seamless information flow and extraction across layers. This hierarchical encoding approach ensures that the GNN effectively captures the structural and fire-related information necessary for accurate MIDR predictions.

4) *Edge update mechanism:* Traditional GNNs often do not update edge attributes,  $e_{i,j}$ , during the iterative update process in each layer. However, in the context of fire scenarios, the attributes of beams and columns (e.g., material properties and geometric characteristics) evolve with temperature changes, directly affecting the computation of the MIDR. To address this limitation, we introduce an EU module that dynamically updates edge attributes during each layer’s computation. After updating node attributes via message passing in each layer of the GNN, the EU module utilizes the attributes of the two adjacent nodes and the edge itself to update the edge attributes. This ensures that the edge features reflect the ongoing structural changes due to fire conditions.

With the EU module, the standard GNN operation in Equation (8) is modified to include EUs. The updated node attributes are expressed as follows:

$$v_i^k = \gamma^k \left( v_i^{k-1}, \bigoplus_{j \in \mathcal{N}(i)} \phi^k(v_i^{k-1}, v_j^{k-1}, e_{j,i}^{k-1}) \right), \quad (9)$$

The EU module updates the edge attributes as follows:

$$e_{j,i}^k = \zeta(v_i^k, v_j^k) + e_{j,i}^{k-1}. \quad (10)$$

where  $\zeta(\cdot)$  is the update function for edge attributes, implemented as a single-hidden-layer MLP.

The inclusion of the EU module enables:

- 1) **Dynamic adaptation:** Capture temperature-induced changes in beam and column properties during each layer’s computation.
- 2) **Enhanced modeling:** Simultaneously updates node and edge attributes, resulting in a more accurate representation of the structural state.
- 3) **Improved performance:** Provides the GNN with the ability to better model the structural transformations under fire scenarios, leading to more precise MIDR predictions.

By iteratively updating edge attributes, the EU module effectively integrates the evolving structural properties into the GNN, enhancing its predictive capabilities in fire scenarios.

### B. TL-based Network Training

The proposed GNN framework computes an embedding vector for each node. To predict the IDR, an additional MLP is employed to map the node embedding vector to the corresponding IDR value. We explore two baseline training and inference methods, referred to as Strawman 1 and Strawman 2, as illustrated in Figure 7:

- **Strawman 1:** This approach aggregates all node embeddings in a graph into a single graph embedding using a *pooling operation*. The graph embedding is then used to predict the structure’s MIDR.
- **Strawman 2:** In this approach, the IDR for each node is directly predicted using its embedding, and the maximum value is selected as the structure’s MIDR.

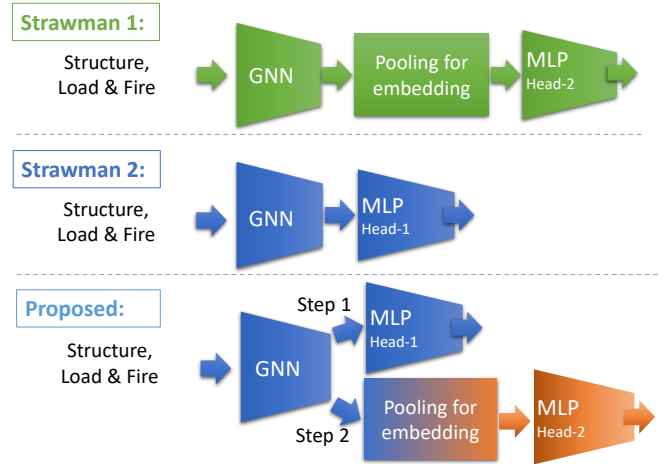


Fig. 7: Comparison of different training strategies. Head-1 and Head-2 represent the MLPs for different tasks, such as predicting the IDR of each node in a structure and the MIDR of a structure.

While Strawman 1 focuses solely on predicting the MIDR, it fails to leverage the IDR labels available for individual

nodes data. Consequently, this approach risks overfitting when the dataset is small. On the other hand, Strawman 2 makes use of all node-level IDR labels, but the inclusion of non-MIDR nodes during training may dilute the model’s focus on predicting the MIDR. To overcome these limitations, we propose a TL-based training method that integrates the strengths of both approaches. By framing the problem as two related tasks –predicting node-level IDRs and structure-level MIDR– we adopt a multi-task TL approach with a two-step training procedure, as illustrated in Figure 7.

In the first step, the GNN is trained to predict the IDR of individual nodes, using an MLP referred to as **task head-1**, used in Strawman 2, Figure 7. During this step, the GNN learns to extract global structural features. The loss function for this step is defined as follows:

$$L_{\text{task-1}}(\Theta_{\text{GNN}}, \Theta_{\text{head-1}}) = \frac{1}{\sum_{m=1}^M N_m I_m} \sum_{m=1}^M \sum_{n=1}^{N_m} \sum_{i=1}^{I_m} \left( d_{m,n,i}^{\text{gt}} - \hat{d}_{m,n,i} \right)^2, \quad (11)$$

where  $d_{m,n,i}^{\text{gt}}$  is the ground truth IDR for node  $i \in (1, 2, \dots, I_m)$  in structure  $m \in (1, 2, \dots, M)$  computed via OpenSeesRT under fire scenario  $n \in (1, 2, \dots, N_m)$ ,  $\hat{d}_{m,n,i}$  represents the predicted IDR from the model,  $\Theta_{\text{GNN}}$  is the set of parameters of the GNN, and  $\Theta_{\text{head-1}}$  is the set of parameters of task head-1. The optimization objective for this step is as follows:

$$\min_{\Theta_{\text{GNN}}, \Theta_{\text{head-1}}} L_{\text{task-1}}(\Theta_{\text{GNN}}, \Theta_{\text{head-1}}). \quad (12)$$

In the second step, the trained GNN parameters from the first step are reused as a *feature extractor*. The MLP for node-level IDR prediction (task head-1) is replaced with a new MLP, referred to as **task head-2**, used in Strawman 1, Figure 7, to predict the MIDR of the structure. During this step, task head-2 is first trained independently, followed by *fine-tuning* the entire GNN. We define the MIDR for the  $m$ -th structure under fire scenario  $n$  as follows:

$$d_{m,n,\text{max}} \triangleq \max_{i=1,2,\dots,I_m} d_{m,n,i}. \quad (13)$$

The loss function for this step is defined as follows:

$$L_{\text{task-2}}(\Theta_{\text{GNN}}, \Theta_{\text{head-2}}) = \frac{1}{\sum_{m=1}^M N_m} \sum_{m=1}^M \sum_{n=1}^{N_m} \left( d_{m,n,\text{max}}^{\text{gt}} - \hat{d}_{m,n,\text{max}} \right)^2, \quad (14)$$

where  $d_{m,n,\text{max}}^{\text{gt}}$  denotes the ground truth MIDR for the  $m$ -th structure under fire scenario  $n$  computed using OpenSeesRT,  $\hat{d}_{m,n,\text{max}}$  represents the predicted MIDR from the model, and  $\Theta_{\text{head-2}}$  is the set of parameters of task head-2. The optimization objective for this step is as follows:

$$\min_{\Theta_{\text{GNN}}, \Theta_{\text{head-2}}} L_{\text{task-2}}(\Theta_{\text{GNN}}, \Theta_{\text{head-2}}). \quad (15)$$

The proposed TL-based methods offers these benefits:

- 1) **Effective utilization of data:** Leverage node-level IDR labels while focusing on MIDR prediction.

- 2) **Improved generalization:** Enhances the model’s ability to generalize across diverse fire scenarios and structural configurations.
- 3) **Accurate MIDR predictions:** Integrates global structural information for precise MIDR predictions, outperforming the individual Strawman methods.

By combining node-level and structure-level predictions in a two-step training pipeline, the TL-based approach achieves a robust balance between learning granular details and capturing global structural patterns.

## VI. MOST FIRE-SENSITIVE POINT PREDICTOR

With the training of the MIDR Predictor complete, we have developed a neural network-based agent model that effectively serves as a surrogate for the FEA conducted using OpenSeesRT. This agent model presents two critical advantages over traditional FEA: computational efficiency and differentiability. These advantages are leveraged fully in the training of the MFSP Predictor, which is designed to identify the the location within the building structure that exhibits the highest vulnerability under fire conditions, as indicated by the MIDR. Importantly, the training process for the MFSP Predictor no longer depends on direct FEA results. Instead, the fixed parameters of the pretrained MIDR Predictor are utilized as a computational foundation. This allows the MIDR Predictor to remain unchanged during the MFSP Predictor’s training, ensuring consistency and efficiency in the workflow. By relying solely on the outputs of the MIDR Predictor, the MFSP Predictor benefits from the speed and differentiability of the agent model while eliminating the need for repeated computationally expensive FEA simulations.

### A. Pseudo-Labeling and Loss Choice

As illustrated in Figure 1, the MFSP Predictor operates as the “argmaxer” of the MIDR Predictor. An intuitive choice for the loss function is to minimize the negative output of the MIDR Predictor, denoted as  $L_{\text{MIDR}}$ . This loss leverages the differentiable nature of the MIDR Predictor as an agent and is expressed as follows:

$$L_{\text{MIDR}} = -\frac{1}{\sum_{m=1}^M N_m} \sum_{m=1}^M \sum_{n=1}^{N_m} \hat{d}_{m,n,\text{max}}, \quad (16)$$

where  $\hat{d}_{m,n,\text{max}}$  represents the MIDR predicted by the MIDR Predictor for the  $n$ -th fire scenario in the  $m$ -th structure.

This approach conceptually resembles the Actor-Critic framework in Reinforcement Learning (RL) [26]: the MFSP Predictor acts as the “Actor”, proposing actions in the form of fire points, while the MIDR Predictor serves as the “Critic”, evaluating the quality of the Actor’s actions. However, similar to challenges in RL, this method can lead to poor training outcome or convergence issues. The MIDR Predictor is a complex function, and optimizing its output through gradient descent often results in local optima or unstable training. Additionally, the fixed nature of MIDR Predictor limits the ability to introduce randomness for balancing exploration and exploitation, a core mechanism in RL.

To address these issues, we propose an alternative approach inspired by the computational efficiency of the MIDR Predictor. Instead of directly using  $L_{\text{MIDR}}$ , we use the MIDR Predictor to generate pseudo ground truths for the MFSP. This process is depicted in Figure 8. Specifically, at the granularity of rooms, we consider the center point of each room in a building as a potential fire point. The MIDR Predictor is used to estimate the MIDR for each fire point, and the fire point with the highest MIDR selected as the pseudo ground truth MFSP for the building. This pseudo-labeling approach allows efficient labeling of unlabeled data at room-level granularity.

For a given  $m$ -th building structure, let the pseudo ground truth MFSP coordinates be  $(x_m^{\text{pgt}}, y_m^{\text{pgt}}, z_m^{\text{pgt}})$ , with a corresponding MIDR  $\hat{d}_m^{\text{pgt}}$ . Using this pseudo-labeling, we define the Mean Squared Error (MSE) loss as follows:

$$L_{\text{MSE}} = \frac{1}{M} \sum_{m=1}^M \left( (x_m^{\text{pgt}} - \hat{x}_m)^2 + (y_m^{\text{pgt}} - \hat{y}_m)^2 + (z_m^{\text{pgt}} - \hat{z}_m)^2 \right), \quad (17)$$

where  $\hat{x}_m$ ,  $\hat{y}_m$ , and  $\hat{z}_m$  are the MFSP Predictor’s outputs for the  $m$ -th structure.

Since the pseudo-labeling process provides ground truth at room-level granularity, it is beneficial to combine  $L_{\text{MIDR}}$  and  $L_{\text{MSE}}$  into a hybrid loss function via a weighted sum to train the MFSP Predictor. The combined loss  $L_{\text{Hybrid}}$  is defined as follows:

$$L_{\text{Hybrid}} = w_1 L_{\text{MIDR}} + w_2 L_{\text{MSE}}, \quad (18)$$

where  $w_1$  and  $w_2$  are weights balancing the contributions of the two loss components. In this study, we fix  $w_2 = 1$ , so that  $w_1$  can be interpreted as a measure of the trust or reliance on the pseudo ground truth MFSP generated by the labeling process: the reliance increases as  $w_1$  decreases. This hybrid approach combines the strengths of leveraging differentiability through  $L_{\text{MIDR}}$  and the guidance provided by pseudo ground truth through  $L_{\text{MSE}}$ , offering a robust method for training the MFSP Predictor.

### B. TL with GNN in MIDR Predictor

The MFSP Predictor operates as an “argmaxer” for the MIDR Predictor. While it could be designed as a completely new network and trained from scratch (i.e., De novo training), we propose leveraging the pretrained GNN module from the MIDR Predictor through TL. The GNN module in the MIDR Predictor has already captured comprehensive global structural information, making it an foundation for the MFSP Predictor. Specifically, we reuse the GNN module as a feature extractor, replace the MLP task head with a new one tailored for the MFSP task, and fine-tune the entire model to optimize its performance.

1) *Structural information via TL:* By reusing the pretrained GNN module, which encodes essential structural and gravity load features, the MFSP Predictor can focus on learning the relationships necessary to identify the MFSP. This approach reduces training time and enhances model performance by

building on the already-learned representations of structural information, rather than starting from scratch.

2) *The virtual fire point method:* A unique challenge arises due to the way the GNN module processes inputs. In addition to structural and gravity load data, the GNN also requires a fire location input. Common masking techniques, such as zero-value masking (i.e., ignore certain inputs by setting them to zero) used in computer vision or natural language processing, cannot be directly applied here. This is because the coordinates  $(0, 0, 0)$  represent a valid location –specifically, a fire at the bottom corner of the building structure. Thus, zero-value masking is unsuitable for this context.

To overcome this limitation, we introduce a randomized Virtual Fire Point (VFP) method. During training, a random virtual fire location is assigned to each structure for every iteration, independently of prior iterations. This randomized approach forces the network to learn the global structural features necessary for predicting the MFSP, while effectively ignoring the influence of specific fire locations.

3) *Generalization and inference:* During inference, the network no longer relies on actual fire locations but uses a predefined VFP to generalize its predictions. For evaluation purposes, we set the VSP to the geometric center of the structure. This ensures that the MSFP Predictor focuses on the overall structural information rather than being biased by the presence of specific fire locations. By combining TL and the VFP method, the MFSP Predictor achieves robust generalization and improved accuracy in identifying the MFSP within diverse structural configurations.

## VII. MODEL IMPLEMENTATION AND EVALUATION

This section outlines the implementation details and evaluates the performance of both the MIDR and MFSP Predictors.

### A. MIDR Predictor Evaluation

1) *Implementation details:* To explore the impact of model capacity on performance, we implemented two versions of the MIDR Predictor: the *small predictor* and the *large predictor*. Both models share an identical network architecture but differ in the dimensions of the embedding vectors used for graph nodes and edges. Specifically, the small predictor employs an embedding dimension of 32, while the large predictor employs an embedding dimension of 64. These variations allow us to evaluate the trade-offs between model complexity, computational efficiency, and predictive accuracy.

The detailed configurations of each network component, all utilizing ReLU as the activation function in their MLP layers, are outlined below:

- **Initial Encoders for Nodes and Edges:** Two distinct single-hidden-layer MLPs serve as encoders for nodes and edges, each tailored to its respective input features. The dimensions of their hidden layers are set to be the same as the output dimension. Consequently, for the small predictor, where both the node and edge embedding dimensions are set to 32, the node encoder layers are configured as  $[13, 32, 32]$  for the input features, hidden

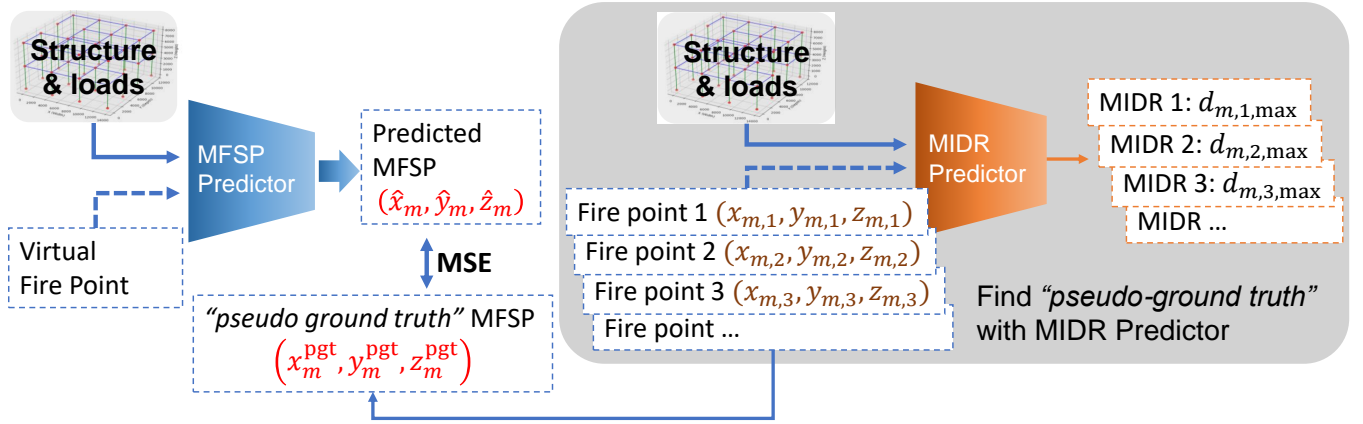


Fig. 8: Procedure of pseudo-labeling for the  $m$ -th building structure.

layer, and output layer, respectively. Similarly, the edge encoder layers are [9, 32, 32]. Refer to Section V-A3 for the input attribute counts. For the large predictor, the embedding dimensions are increased to 64, and the layer configurations are adjusted accordingly. This design ensures the encoders effectively process distinct feature sets for nodes and edges while seamlessly integrating with the GNN architecture.

- **Message Function,  $\phi^k(\cdot)$ :** A single-hidden-layer MLP is used for the message function. Its input is the concatenation of the embeddings of the source node and the edge. The output dimension matches the node embedding dimension. For the small predictor, the hidden layer dimension is 64, while for the large predictor, it is 128.
- **Aggregation Operation,  $\oplus$ :** The “max” function is used as the aggregation operation. It selects the maximum value from the neighboring node messages. This approach (compared to other aggregation methods through averaging or summation) aligns with a conservative engineering design philosophy, prioritizing the most critical structural information for robust analysis and decision-making.
- **Update Function,  $\gamma^k(\cdot)$ :** The update function combines the previous node embedding with the processed aggregated message. Specifically, the aggregated message for node  $i$ , denoted as  $\tilde{v}_i^k$ , is processed through a single-hidden-layer MLP,  $\tilde{\gamma}^k(\cdot)$ , whose output dimension matches the node embedding dimension. The update rule is given as follows:

$$\gamma^k \left( \mathbf{v}_i^{k-1}, \tilde{v}_i^k \right) = \mathbf{v}_i^{k-1} + \tilde{\gamma}^k \left( \tilde{v}_i^k \right). \quad (19)$$

For the small predictor, the hidden layer dimension of  $\tilde{\gamma}^k(\cdot)$  is 64, while for the large predictor, it is 128.

- **Edge Update (EU) Function,  $\zeta(\cdot)$ :** A single-hidden-layer MLP is used for updating edge attributes. The input is the concatenation of the two adjacent nodes. Thus, the input dimension is twice the node embedding dimension. The output dimension corresponds to the edge embedding dimension. For the small predictor, the hidden

layer dimension is 32, while for the large predictor, it is 64.

- **Task Head-1, Task Head-2, and Pooling Function:** Task heads are implemented as linear layers. The pooling function combines node embedding into a graph embedding by concatenating the mean and max pooling results. Consequently, the input dimension for task head-1 is twice the node embedding dimension, while for task head-2, it equals the node embedding dimension. Recall that task head-1 and task head-2 predict the IDR as a node-level outcome and MIDR as a structure-level outcome, respectively, i.e., a scalar value is output as the final prediction for each head.

The number of layers in the GNN is aligned with the number of stories in the building structure. As the maximum number of the stories of the considered buildings in this study is 7 (refer to Section IV-A), we set the GNN to possess 7 layers. Note that to process a  $k$ -story structure, only first  $k$  layers of the entire GNN is used (refer to Section V-A2). For the small predictor configuration, the total parameter count is approximately  $7.1 \times 10^4$ , while for the large predictor configuration, it reaches about  $2.8 \times 10^5$ . In the absence of the EU functionality, the parameter counts are marginally reduced to approximately  $6.8 \times 10^4$  for the small predictor and  $2.7 \times 10^5$  for the large predictor.

2) *Evaluation metrics:* We evaluate the performance of the MIDR Predictor using three metrics: Mean Squared Error (MSE), Mean Absolute Error (MAE), and Spearman’s rank correlation coefficient. MSE, defined in Equation (17), quantifies the squared difference between predicted and ground truth MIDRs. MAE measures the absolute difference and is defined as:

$$L_{\text{MAE}} = \frac{1}{\sum_{m=1}^M N_m} \sum_{m=1}^M \sum_{n=1}^{N_m} \left| \hat{d}_{m,n,\max} - d_{m,n,\max}^{\text{gt}} \right|, \quad (20)$$

where  $d_{m,n,\max}^{\text{gt}}$  is the ground truth MIDR of  $m$ -th structure under the  $n$ -th fire scenario (calculated by OpenSeesRT), and

$\hat{d}_{m,n,\max}$  is the corresponding prediction from the MIDR Predictor.

Since the ultimate goal is to identify the MFSP rather than exact MIDR values, the ranking of MIDRs across different fire scenarios for each structure is critical. For this, we use Spearman’s rank correlation coefficient ( $\rho_s$ ), which measures the *monotonic relationship* between two sequences  $X$  and  $Y$  and is defined as follows:

$$\rho_s(X, Y) \triangleq \rho(R_X, R_Y) = \frac{\text{cov}(R_X, R_Y)}{\sigma_{R_X} \sigma_{R_Y}}. \quad (21)$$

In this formulation,  $R_X$  and  $R_Y$  represent the rank-ordered sequences of  $X$  and  $Y$ , respectively, where each element is replaced by its rank in the sorted sequence. Moreover,  $\rho(\cdot, \cdot)$  denotes the Pearson correlation coefficient,  $\text{cov}(R_X, R_Y)$  represents the covariance of  $R_X$  and  $R_Y$ , which quantifies how changes in rank of  $X$  correspond to changes in rank of  $Y$ , and  $\sigma_{R_X}$  and  $\sigma_{R_Y}$  denote the standard deviations of the rank distributions  $R_X$  and  $R_Y$ , respectively. Unlike Pearson’s correlation, which measures linear relationships, Spearman’s correlation focuses on how well the rank-ordering of the variables aligns. This makes it particularly suitable for ordinal data or nonlinear relationships. The resulting values of  $\rho_s$  range from  $-1$  to  $+1$ , with values closer to  $+1$  indicating strong agreement in rank-ordering, values near  $0$  indicating weak or no correlation, and values closer to  $-1$  indicating a strong inverse correlation.

In this paper, for the  $m$ -th structure with  $N_m$  fire scenarios, we compute  $\rho_s(X, Y)$  between the sequence of ground truth results,  $X \equiv \{d_{m,1,\max}^{\text{gt}}, d_{m,2,\max}^{\text{gt}}, \dots, d_{m,N_m,\max}^{\text{gt}}\}$ , obtained from OpenSeesRT simulations and the sequence of predictions,  $Y \equiv \{\hat{d}_{m,1,\max}, \hat{d}_{m,2,\max}, \dots, \hat{d}_{m,N_m,\max}\}$ , produced by the MIDR Predictor. The final evaluation metric is the average  $\rho_s$  across all structures, providing a robust measure of prediction quality for MFSP identification.

3) *Evaluation results:* For training and evaluating the MIDR Predictor, we exclusively use the labeled dataset, splitting it into 80% for training and 20% for testing. Various neural network configurations and training methods were compared, with the results summarized in Table V.

TABLE V: Evaluation results of the MIDR Predictor (numbers in boldface indicate best results).

Method	Network	MAE	MSE	$\rho_s$
Strawman 1		1.017	1.707	0.162
Strawman 2: No EU		0.320	0.232	0.670
Strawman 2: EU	Small	0.314	0.203	0.689
Proposed: No EU		0.300	0.201	0.685
<b>Proposed: EU</b>		<b>0.278</b>	<b>0.170</b>	<b>0.725</b>
Strawman 1		0.305	0.202	0.649
Strawman 2: No EU		0.305	0.201	0.678
Strawman 2: EU	Large	0.317	0.216	0.704
Proposed: No EU		0.289	0.175	0.707
<b>Proposed: EU</b>		<b>0.272</b>	<b>0.169</b>	<b>0.742</b>

In Table V, the methods Strawman 1, Strawman 2, and Proposed are described in Section V-B and illustrated in

Figure 7. For Strawman 2 and Proposed methods, we further assess the impact of enabling the EU functionality. Two key observations are summarized below:

- **EU functionality:** Comparisons between cases with and without EU reveal that enabling EU consistently enhances model performance. Specifically, the inclusion of EU increases  $\rho_s$  in all cases, and reduces both MAE and MSE for not only the proposed predictors but also the Strawman 2 predictor based on small network.
- **Proposed method:** Among all configurations, the proposed method with EU achieves the best performance, with  $\rho_s$  scores of 0.725 and 0.742 for the small and large networks, respectively. This indicates that the proposed method better captures the structural sensitivity ranking across various fire scenarios when predicting the MIDR.

Figure 9(a) presents the Complementary Cumulative Distribution Function (CCDF) of  $\rho_s$ , i.e.,  $\bar{\mathcal{F}}_{\rho_s}(a) = \mathcal{P}(\rho_s \geq a)$ , where  $\mathcal{P}$  indicates the probability, for the proposed method with EU. Key observations include:

- For predictors using small and large networks (solid lines), namely small and large predictors for simplicity, 83.2% of structures achieve a  $\rho_s$  value greater than 0.50, and 64.4% (small predictor) and 66.7% (large predictor) of structures achieve a  $\rho_s$  value exceeding 0.75. Additionally, large predictor improves on the worst case, where the smallest  $\rho_s$  value increases from  $-0.86$  for small predictor to  $-0.58$  for large predictor.
- MIDR predictors perform much better on severe cases (dashed lines), defined for a structure as a condition where the ground truth MIDR exceeds 2% under at least one fire case. This is in comparison with all cases (solid lines). In severe cases, for the small predictor, 98.0% of structures achieve a  $\rho_s$  value greater than 0.5, and 89.3% exceed 0.75 with an average of 0.90. For the large predictor, 98.7% of structures achieve a  $\rho_s$  value greater than 0.5, while 90.0% exceed 0.75 with an average of 0.91.

These results indicate that the proposed method performs exceptionally well under severe cases. This is consistent with our expectations: when building structures are less sensitive to fire, errors in MIDR prediction have a relatively small impact. However, the risk of MIDR prediction errors becomes critical when structures are sensitive to fire.

To provide a more intuitive understanding of the proposed method’s performance, we present the ground truth MIDR and predicted MIDR for three example structures under the small predictor (Figure 9(b)) and the large predictor (Figure 9(c)). In these examples, ex1 and ex2 represent severe cases, while ex3 remains relatively stable with low MIDR across all fire scenarios. From these figures, for both predictors, the predicted results for ex1 and ex2 closely match the ground truth, achieving  $\rho_s$  values above 0.92. For ex3, the performance of both predictors is lower but the large predictor outperforms the small predictor, achieving a  $\rho_s$  value above 0.7.

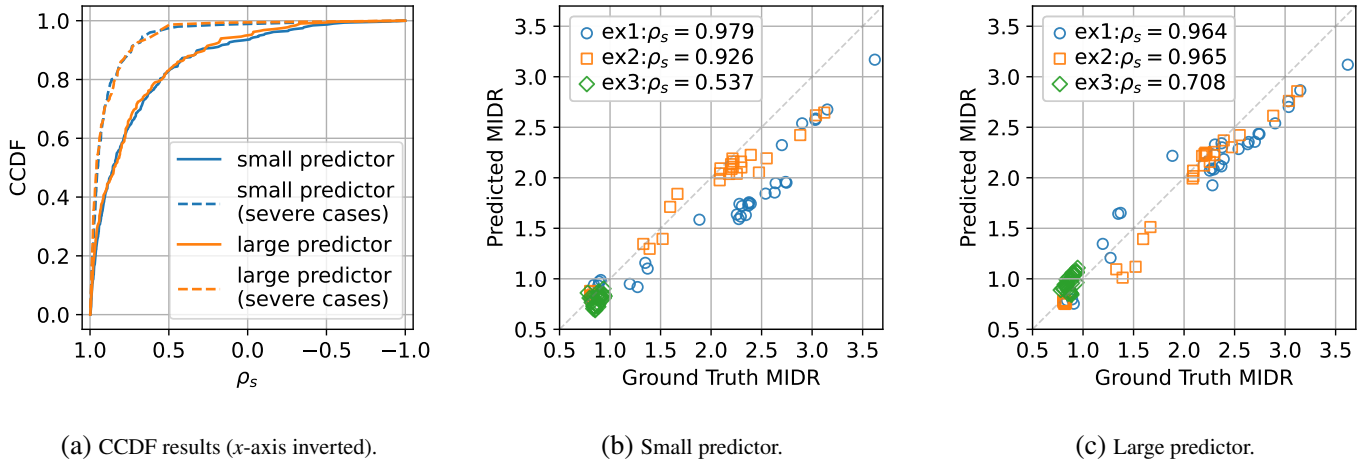


Fig. 9: Representative MIDR Predictor results: (a) CDF of  $\rho_s$  of proposed MIDR Predictors for two different sizes (severe cases for structures whose ground truth MIDR is larger than 2% in at least one fire case); (b) and (c) show the ground truth and predicted MIDR of 3 example structures (ex1, ex2 & ex3) for the small and large predictors, respectively.

In conclusion, the proposed method with EU functionality demonstrates exceptional performance across all metrics, particularly for severe cases, where accurate MIDR prediction is most critical. These findings highlight the robustness and effectiveness of the proposed method in supporting fire safety assessments for building structures.

### B. MFSP Predictor Evaluation

To evaluate the MFSP Predictor, we adopt the proposed method with EU as the final model for the MIDR Predictor and utilize it to train the MFSP Predictor. As described in Section VI-B, we consider two training strategies for the MFSP Predictor:

- 1) **De novo training:** Training a completely new network from scratch.
- 2) **TL with GNN:** Reusing the GNN module, including the initial encoders, from the MIDR Predictor.

Additionally, two loss functions are evaluated:

- 1) **MSE loss:** Mean squared error focusing on accuracy of predicted coordinates.
- 2) **Hybrid loss:** A combination of MSE loss and the MIDR-based loss for better ranking consistency.

This section compares the performance of these four combinations. The network architecture of the MFSP Predictor is almost identical to that of the MIDR Predictor, consisting of an initial encoder, a GNN, pooling layers, and an MLP task head. There are only a few differences:

- **Final MLP Head:** The task head in MFSP Predictor replaces the linear layer in the MIDR Predictor with a single-hidden-layer MLP. The hidden layer’s dimension matches the graph embedding (twice the node embedding dimension), and the output layer has a dimension of 3, representing the predicted coordinates  $(x, y, z)$ . A “sigmoid” activation function is applied to normalize the predicted coordinates to the range  $(0, 1)$ , aligning with the building normalized spatial dimensions.

- **De Novo training:** The initial node input features include only the spatial coordinates of the nodes. Fire point information is excluded, as no prior knowledge from the MIDR Predictor is utilized.
- **TL with GNN training:** The GNN module and initial encoders from the MIDR Predictor are directly reused. Moreover, the fire point information is replaced with a VFP to ensure consistency in input structure. This enables the network to generalize its understanding of structural information without relying on specific fire locations.

By evaluating these configurations and loss functions, the MFSP Predictor aims to efficiently and accurately predict the MFSP within the building.

1) *Evaluation metrics:* In Section VI-A, we introduce the “Pseudo-Labeling” method, which generates pseudo ground truth coordinates for the MFSP. These pseudo-labels are used to evaluate the MFSP Predictor through various metrics, capturing both point-level and room-level performances.

For a given  $m$ -th structure, the distance error between predicted MFSP and pseudo ground truth MFSP is defined as:

$$e_m = \sqrt{(x_m^{\text{pgt}} - \hat{x}_m)^2 + (y_m^{\text{pgt}} - \hat{y}_m)^2 + (z_m^{\text{pgt}} - \hat{z}_m)^2}, \quad (22)$$

where  $\hat{x}_m, \hat{y}_m, \hat{z}_m$  represent the  $x, y, z$  coordinates predicted by the MFSP Predictor, while  $x_m^{\text{pgt}}, y_m^{\text{pgt}}, z_m^{\text{pgt}}$  denote the pseudo ground truth MFSP coordinates obtained using the MIDR Predictor. This metric provides a direct measure of the prediction accuracy at the point level. However, as the pseudo ground truth is defined at a room-level granularity, its reliability may vary depending on the building’s size and complexity.

To align the evaluation with practicality, two room-level metrics are introduced: room distance error and room rank. These metrics treat rooms as the basic unit of measurement,

reflecting how well the MFSP Predictor identifies the MFSR, defined as the room where MFSP is located.

**Room distance error** measures the distance between the predicted MFSR and the pseudo ground truth MFSR, assuming all edges (beams and columns) of the building structure have unit length. For the  $m$ -th structure, the room dimensions are defined as  $\tilde{x}_m, \tilde{y}_m, \tilde{z}_m$  for the respective length, width, and height of each room. The coordinates of the center point of the predicted MFSR is denoted as  $(\hat{x}'_m, \hat{y}'_m, \hat{z}'_m)$ . The room distance is then computed as:

$$\tilde{e}_m = \sqrt{\left(\frac{x_m^{\text{pgt}} - \hat{x}'_m}{\tilde{x}_m}\right)^2 + \left(\frac{y_m^{\text{pgt}} - \hat{y}'_m}{\tilde{y}_m}\right)^2 + \left(\frac{z_m^{\text{pgt}} - \hat{z}'_m}{\tilde{z}_m}\right)^2}. \quad (23)$$

This metric provides a scaled distance measure, accounting for the room size and structure dimensions.

**Room rank** evaluates the ranking of the room containing the predicted MFSP based on pseudo-labeled MIDR values. For the  $m$ -th structure with  $N_m$  rooms (i.e.,  $N_m$  pseudo fire cases), the pseudo-labeled MIDRs are sorted in descending order, indexed by the fire case occurring at each room’s center point, i.e.,  $d_{m,1,\text{max}}^{\text{pgt}} > d_{m,2,\text{max}}^{\text{pgt}} > \dots > d_{m,N_m,\text{max}}^{\text{pgt}}$ . If the predicted MFSP falls into the  $l$ -th ranked room, the room rank is defined as  $r_m = l$ . Lower ranks indicate better prediction performance, as the predicted MFSR is closer to the MFSP.

In addition to the distance error, room distance error, and room rank, the predicted MIDR at the identified MFSP can also serve as an evaluation metric. Higher MIDR values reflect the Predictor’s ability to identify the MFSPs, directly correlating with the severity of the structural response.

These evaluation metrics collectively assess the MFSP Predictor’s performance, balancing point-level precision, room-level granularity, and the functional implications of predictions. The inclusion of room distance error and room rank ensures that the evaluation aligns with practical building-level assessments, where rooms are typically used reference units for structural analysis and fire safety planning.

2) *Evaluation results:* Using the metrics defined in the previous section, we evaluate the performance of the MFSP Predictor by calculating average quantities across all structures. Since MIDR Predictor provides a computationally efficient agent model to rapidly generate pseudo labels for unlabeled data, the large unlabeled dataset can be effectively utilized for training the MFSP Predictor. For this evaluation, the unlabeled dataset is divided into 80% for training and 20% for testing. The evaluation results for various training methods and loss functions are summarized in Table VI. For the “Hybrid loss”, the weight for the MSE term is fixed at  $w_2 = 1 \text{ m}^{-2}$ , while the weight for the MIDR term is varied as  $w_1 = 10, 50, \text{ or } 100$ , as described in Equation (18). In Table VI, the TL with GNN results for  $w_1 = 50$ , using both small and large networks, are taken as the reference cases for the listed multipliers in parentheses.

Comparing the De novo training and TL with GNN methods, we observe that the TL with GNN approach outperforms De novo training in all metrics. For both small and large pre-

dictors, TL with GNN achieves lower average distance error, average room distance error, and average room rank, while also attaining higher average MIDR values compared to De novo training using the same loss function. This indicates that the TL with GNN approach effectively leverages the information embedded in the MIDR Predictor’s GNN module, significantly enhancing the performance of the MFSP Predictor.

We compare the MSE loss with Hybrid loss within the TL with GNN method, using the Hybrid ( $w_1 = 50$ ) case as an example. For the average MIDR metric, the Hybrid loss explicitly calculates MIDR, achieving a higher value than the MSE loss by up to  $(2.46 - 2.40) / 2.40 = 2.50\%$  for the small predictor, with a smaller improvement observed for the large predictor. Conversely, as the MSE loss is computed based on the pseudo ground truth MFSP (similar to the distance error metric), it achieves a lower average distance error than that of the Hybrid loss by up to 16% for the large predictor. Interestingly, despite the average room distance error and room rank being calculated relative to the pseudo ground truth MFSP, the Hybrid loss performs similarly to or even better than the MSE loss. This can likely be attributed to the pseudo labels being accurate at the room-level granularity, even though the MFSP is not necessarily located at the exact center of a room. As a result, the MSE and Hybrid loss methods show varying performances across the distance error and room distance error metrics.

The Hybrid loss introduces a trade-off between achieving higher MIDR and lower distance error by adjusting the weights  $w_1$  and  $w_2$ , which reflect the degree of reliance on the pseudo labels. In this analysis, the weight for the MSE term is fixed at  $w_2 = 1$ . By varying the weight for the MIDR term ( $w_1$ ) from 10 to 100, the reliance on pseudo labels decreases as  $w_1$  increases. This trade-off is evident when comparing results for  $w_1 = 10$  and  $w_1 = 50$ :  $w_1 = 10$  results in approximately 10% lower distance error but also yields a slightly lower MIDR, reduced by about 1%. However, when  $w_1$  is set to a very large value, such as  $w_1 = 100$ , the reliance on the pseudo labels becomes minimal, and the difficulty of training an “argmax”, as discussed in Section VI-A, negatively impacts the MFSP Predictor’s performance. Notably, even for the average MIDR metric, the performance with  $w_1 = 100$  is worse than that achieved with  $w_1 = 50$ .

Taking TL with GNN and Hybrid loss ( $w_1 = 50$ ) as an example, the average room distance error reaches 1.15, indicating that the predicted MFSP is, on average, located within 1.15 rooms of the ground truth MFSP. Additionally, the average room rank is 6.73 indicating that the predicted MFSP is approximately the 6th or 7th most fire-sensitive room among all rooms in the building structure, with an average of over 87 rooms in each structure in this study. These low values suggest that the MFSP Predictor can accurately identifies the MFSPs in the building.

To further illustrate the performance of the MFSP Predictor, we plotted the Cumulative Distribution Function (CDF), defined as  $\mathcal{F}_X(a) = \mathcal{P}(X \leq a)$ , where  $\mathcal{P}$  indicates the probability and  $X$  is a random variable representing the

TABLE VI: Evaluation results of MFSP Predictor for different training methods and loss functions (numbers in boldface indicate best results).

Method	Loss	Network	Avg. Distance Error (m)	Avg. Room Distance Error	Avg. Room Rank	Avg. MIDR (%)	
De novo training	MSE	Small	5.49 (0.93×)	1.28 (1.08×)	9.09 (1.14×)	2.40 (0.98×)	
De novo training	Hybrid ( $w_1 = 10$ )		5.65 (0.96×)	1.25 (1.06×)	9.11 (1.15×)	2.42 (0.98×)	
De novo training	Hybrid ( $w_1 = 50$ )		6.10 (1.04×)	1.24 (1.05×)	8.50 (1.07×)	2.45 (1.00×)	
De novo training	Hybrid ( $w_1 = 100$ )		6.26 (1.06×)	1.23 (1.04×)	8.59 (1.08×)	2.42 (0.99×)	
TL with GNN	MSE		<b>5.18 (0.88×)</b>	1.21 (1.03×)	8.51 (1.07×)	2.40 (0.98×)	
TL with GNN	Hybrid ( $w_1 = 10$ )		5.31 (0.90×)	<b>1.18 (1.00×)</b>	8.19 (1.03×)	2.43 (0.99×)	
TL with GNN	Hybrid ( $w_1 = 50$ )		5.89 (1.00×)	<b>1.18 (1.00×)</b>	<b>7.95 (1.00×)</b>	<b>2.46 (1.00×)</b>	
TL with GNN	Hybrid ( $w_1 = 100$ )		6.16 (1.05×)	1.21 (1.03×)	<b>7.95 (1.00×)</b>	2.45 (1.00×)	
De novo training	MSE		Large	5.41 (0.92×)	1.27 (1.10×)	8.02 (1.19×)	2.37 (0.97×)
De novo training	Hybrid ( $w_1 = 10$ )			5.64 (0.96×)	1.25 (1.09×)	7.58 (1.13×)	2.40 (0.98×)
De novo training	Hybrid ( $w_1 = 50$ )	6.21 (1.06×)		1.22 (1.06×)	6.96 (1.03×)	2.43 (0.99×)	
De novo training	Hybrid ( $w_1 = 100$ )	6.46 (1.10×)		1.23 (1.07×)	7.27 (1.08×)	2.42 (0.99×)	
TL with GNN	MSE	<b>4.93 (0.84×)</b>		<b>1.15 (1.00×)</b>	7.18 (1.07×)	2.40 (0.98×)	
TL with GNN	Hybrid ( $w_1 = 10$ )	5.21 (0.89×)		<b>1.15 (1.00×)</b>	7.12 (1.06×)	2.41 (0.98×)	
TL with GNN	Hybrid ( $w_1 = 50$ )	5.87 (1.00×)		<b>1.15 (1.00×)</b>	<b>6.73 (1.00×)</b>	<b>2.45 (1.00×)</b>	
TL with GNN	Hybrid ( $w_1 = 100$ )	6.23 (1.06×)		1.18 (1.03×)	7.20 (1.07×)	2.43 (0.99×)	

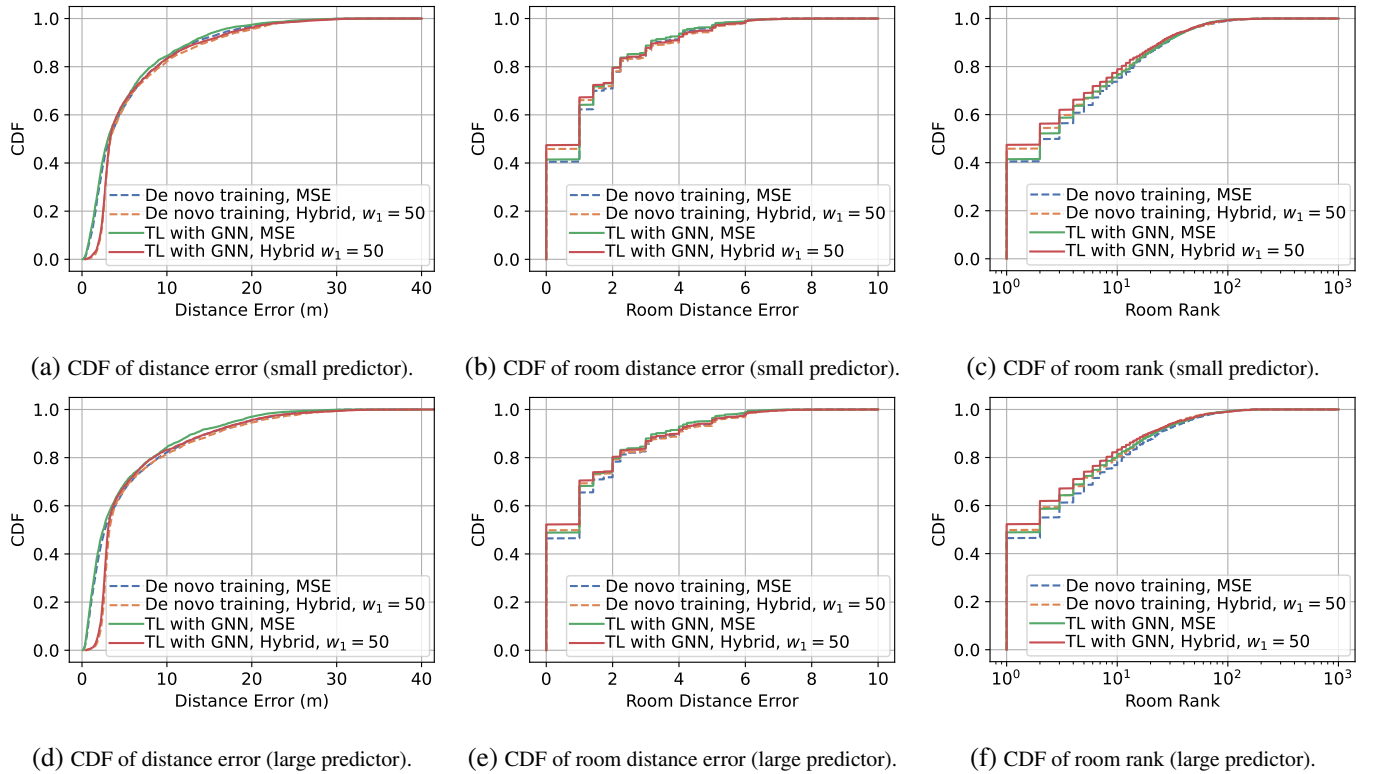


Fig. 10: CDF of distance error, room distance error, and room rank for the small (a to c) and large (d to f) MFSP predictors.

different metrics, i.e., distance error, room distance error, and room rank. Figures 10(a to c) display the results for the small predictor, while Figures 10(d to f) present the results for the large predictor. The key CDF values are also summarized in Table VII. In Figure 10, the CDF curves of TL with GNN generally lie above those of De novo training, demonstrating that the TL with GNN approach outperforms De novo training in most cases. Besides, TL with GNN requires much less computational resources in training to achieve this advantage. This is because it leverages a pre-trained GNN, which significantly

reduces the computational burden of training from scratch. The pre-trained model provides a well-initialized starting point, requiring only fine-tuning to adapt to the target task. This further highlights the efficiency and superiority of the approach of TL with GNN.

Specifically, as detailed in Table VII, for the small network using TL with GNN and Hybrid loss ( $w_1 = 50$ ), 65.40% of cases achieve a distance error of less than 5 meters. When the threshold is extended to 10 meters, this ratio increases to 83.21%, surpassing the 82.19% achieved with De novo



TABLE VII: Key CDF values (%) of different metrics to evaluate the MFSP Predictor (numbers in boldface indicate best results).

Method	Loss	Network	$e_m \leq 5m$	$e_m \leq 10m$	$\tilde{e}_m \leq \sqrt{2}$	$\tilde{e}_m \leq 2$	$r_m \leq 5$	$r_m \leq 10$
De novo training	MSE	Small	63.69	83.46	69.95	77.83	63.91	75.24
De novo training	Hybrid ( $w_1 = 50$ )		63.75	82.19	71.10	77.98	66.61	76.83
TL with GNN	MSE		65.28	<b>84.34</b>	71.75	<b>79.66</b>	66.93	76.67
TL with GNN	Hybrid ( $w_1 = 50$ )		<b>65.40</b>	83.21	<b>72.38</b>	79.51	<b>68.98</b>	<b>78.85</b>
De novo training	MSE	Large	66.74	82.16	70.88	78.26	68.58	78.42
De novo training	Hybrid ( $w_1 = 50$ )		66.83	81.63	73.00	79.29	71.57	80.50
TL with GNN	MSE		<b>69.10</b>	<b>84.30</b>	73.47	79.76	72.28	81.47
TL with GNN	Hybrid ( $w_1 = 50$ )		68.10	83.21	<b>73.93</b>	<b>80.32</b>	<b>74.06</b>	<b>83.21</b>

training. Regarding room distance error,  $\tilde{e}_m$ , the large network using TL with GNN and Hybrid loss achieves the highest probability of 73.93% for  $\tilde{e}_m \leq \sqrt{2}$ , indicating that the predicted MFSP is either within the same room as the pseudo ground truth MFSP or an adjacent room. Notably, for normalized rooms treated as unit-length squares (Section VII-B1), the longest distance between the centers of two diagonally adjacent rooms is  $\sqrt{2}$ . When the error threshold is further relaxed to  $\tilde{e}_m \leq 2$ , this probability increases to 80.32%, reflecting a high level of accuracy. For room rank, the large network employing TL with GNN and Hybrid loss achieves the highest Top-5 accuracy, defined as the fraction of instances where the predicted MFSR ranks among the top 5 pseudo ground truth MFSRs, i.e.,  $\mathcal{P}(r_m \leq 5)$ . This accuracy reaches 74.06%, representing an improvement of 2.49% over De novo training. Additionally, when using MSE loss, the TL with GNN method achieves a Top-5 accuracy of 72.28%, which is 3.7% higher than that of De novo training. These results highlight the robustness of the TL with GNN approach, particularly when paired with Hybrid loss, in accurately identifying the most fire-sensitive locations within building structures.

In summary, the TL with GNN approach consistently outperforms De novo training across all evaluation metrics, highlighting the effectiveness of leveraging the MIDR Predictor’s GNN module to enhance the performance of the MFSP Predictor. Two notable trade-offs arise when selecting the loss function. The first is between  $w_1$  and  $w_2$  within the Hybrid loss to include reliance on the room-level granularity of pseudo ground truth MFSP. The second is between MSE loss and Hybrid loss for higher efficiency and accuracy. While the Hybrid loss achieves slightly better results in most metrics (except for distance error), it incurs a higher computational cost due to the additional GNN forward pass required to calculate the MIDR loss and the backward pass through MIDR Predictor to calculate the gradient of the loss  $L_{\text{MIDR}}$ . In contrast, the MSE Loss avoids this additional computational cost, making it more efficient but potentially less accurate in certain scenarios. This trade-off between computational cost and accuracy should be carefully considered based on the specific requirements and constraints of the application. If computational efficiency is a priority, the MSE loss may be more suitable. However, if higher accuracy in identifying sensitive fire points is critical, the Hybrid loss could provide a more robust solution.

## VIII. CONCLUDING REMARKS

This study introduces a neural network-based framework for predicting the Most Fire-Sensitive Point (MFSP) in building structures, advancing fire safety assessment through a novel combination of data-driven and simulation-based approaches. By employing a differentiable agent model, the proposed framework efficiently simulates Finite Element Analysis (FEA) to predict the Maximum Interstory Drift Ratio (MIDR) under fire conditions. This agent model facilitates rapid generation of MFSP-labeled data, directly supporting the training of the MFSP Predictor. Complementing this, a rule-based temperature generation method was developed, enabling the creation of extensive structural and fire simulation datasets. These contributions establish a comprehensive workflow for data generation and neural network training.

Key innovations include the application of Graph Neural Networks (GNNs) to process structural data, the integration of Transfer Learning (TL) to enhance prediction performance, and the introduction of an Edge Update (EU) mechanism to account for property changes in beams and columns during fire scenarios. Experimental evaluations demonstrated the framework’s effectiveness: the MIDR Predictor achieved a maximum average Spearman’s rank correlation coefficient of 0.74, with an average coefficient exceeding 0.91 for severe fire scenarios. The MFSP Predictor, at the room level, attained Top-5 and Top-10 accuracies of up to 74.1% and 83.2%, respectively. These results highlight the potential of the proposed framework to enhance fire safety assessment in buildings.

Despite these achievements, several limitations and opportunities for future research remain. The dataset used in this study, generated through a simplified approach, aligns with real-world scenarios but may not fully capture the complexity of structural geometry or thermal fields under fire conditions. Incorporating real-world measurement data or use of the Fire Dynamics Simulator (FDS) could improve model accuracy. Challenges related to limited data volume could be addressed through TL, domain adaptation, or data augmentation, leveraging trained models from this study as a foundation.

From a modeling perspective, the depth of GNN layers was constrained to match the number of building stories, successfully mitigating over-smoothing issues. However, this constraint may hinder communication between nodes in low-rise, large-area buildings, potentially limiting the model’s

ability to capture horizontal fire spread. Future work could explore alternative architectures, e.g., dummy nodes or enhanced message-passing mechanisms, to overcome such challenges.

Additionally, exploring theoretical connections between GNN performance and FEA tools could provide a more robust theoretical foundation for applying GNNs in structural analysis. Expanding the framework to incorporate other data types, such as image data or OpenSees scripts, could further enhance predictive accuracy and applicability.

Beyond the MFSP prediction task, the proposed framework demonstrates potential for broader applications within civil engineering. The differentiable nature of the MIDR Predictor could be leveraged to tackle other structural challenges, such as identifying the weakest points under gravity and/or lateral loads or detecting regions most susceptible to corrosion. These extensions highlight the versatility of the framework and its potential to address a wide range of structural analysis problems, fostering future innovations in structural safety and resilience.

#### ACKNOWLEDGEMENTS

The authors extend their heartfelt gratitude to Dr. M. Eslami, Mr. G. Zhou, Mr. C.M. Perez, Mr. W. Ruan, Mr. K.T. Pang, and Ms. L. Yang, members of STAIRlab, for their valuable discussions and contributions to this research. Special thanks are due to Prof. S.-L. Huang of Tsinghua University and Prof. L. Zheng of MIT for insightful discussions related to this paper. We are deeply appreciative of the Berkeley Research IT team for providing access to the Savio computing cluster, a vital resource for the “STAIRlab” project. This advanced high-performance computing infrastructure enabled data generation and network training, which were critical to the success of this research. Finally, we gratefully acknowledge the financial support provided to STAIRlab through the Taisei Chair in Civil Engineering at UC Berkeley. Both the computational and financial resources were indispensable completing this work.

#### REFERENCES

- [1] Yngve Anderberg. Modelling steel behaviour. *Fire Safety Journal*, 13(1):17–26, 1988.
- [2] Filipe de Avila Belbute-Peres, Kevin A Smith, Kelsey R Allen, Tenenbaum JB, and JZ Kolter. End-to-end differentiable physics for learning and control. In *32nd Conference on Neural Information Processing Systems (NeurIPS2018)*, Montréal, Canada, 2018.
- [3] California Department of Forestry and Fire Protection, Cal Fire. Statistics on CA wildfires and CAL FIRE activity. <https://www.fire.ca.gov/stats-events/>, Accessed Jan. 9, 2025.
- [4] Hao Cheng and George V. Hadjisophocleous. Dynamic modeling of fire spread in building. *Fire Safety Journal*, 46(4):211–224, May 2011.
- [5] Yuan-Tung Chou, Wei-Tze Chang, Jimmy G. Jean, Kai-Hung Chang, Yin-Nan Huang, and Chuin-Shan Chen. StructGNN: An efficient graph neural network framework for static structural. *Computers & Structures*, 299:107385, August 2024.
- [6] Yong Du and Guo-qiang Li. A new temperature–time curve for fire-resistance analysis of structures. *Fire Safety Journal*, 54:113–120, November 2012.
- [7] Ugur Dundar and Serdar Selamet. Fire load and fire growth characteristics in modern high-rise buildings. *Fire Safety Journal*, 135:103710, February 2023.
- [8] European Committee for Standardization. EN 1993-1-2:2005 (E), 2005. Available from the European Committee for Standardization (CEN).
- [9] Erica Fischer and Walker Maddalozzo. Thermal examples, 2022.

- [10] Jean-Marc Franssen and Venkatesh K Kodur. Fire resistance assessment of concrete structures. *Fire Safety Journal*, 37(3):241–273, 2002.
- [11] Zhongying He, Jianxiang Man, Guolin Li, Haoyang Li, Yifan Song, Tianxing Liu, and Chaojie Song. Study on fire plume and surface temperature field of components in mid through steel box ribbed arch bridge under tanker fire. *Fire Technology*, December 2024.
- [12] A. Hokugo, Y. Hasemi, Y. Hayashi, and Masashi Yoshida. Mechanism for the upward fire spread through balconies based on an investigation and experiments for a multi-story fire in high-rise apartment building. *Fire Safety Science*, 6:649–660, 2000.
- [13] Yuanming Hu, Tzu-Mao Li, Luke Anderson, Jonathan Ragan-Kelley, and Frédo Durand. Taichi: A language for high-performance computation on spatially sparse data structures. *ACM Transactions on Graphics (TOG)*, 38(6):201, 2019.
- [14] International Organization for Standardization. *Fire resistance tests – Elements of building construction – Part 1: General requirements*. ISO, Geneva, Switzerland, 1999. ISO 834-1:1999.
- [15] Yilong Jia, Jun Wang, Wenchi Shou, M. Reza Hosseini, and Yu Bai. Graph neural networks for construction applications. *Automation in Construction*, 154:104984, October 2023.
- [16] Thomas N Kipf and Max Welling. Semi-supervised classification with graph convolutional networks. *arXiv preprint arXiv:1609.02907*, 2017.
- [17] Venkatesh K Kodur and Mazen MB Dwaikat. Response of steel beam–columns exposed to fire. *Engineering Structures*, 32(2):607–619, 2010.
- [18] T.-H. Lee and K. M. Mosalam. Probabilistic fiber element modeling of reinforced concrete structures. *Computers and Structures*, 82(27):2285–2299, 2004.
- [19] Kevin McGrattan, Randall McDermott, Simo Hostikka, and Jason Floyd. *Fire Dynamics Simulator (Version 5) User’s Manual*, 2010. NIST Special Publication 1019-5.
- [20] Kevin B McGrattan, Howard R Baum, Ronald G Rehm, Anthony Hamins, and Glenn P Forney. Fire dynamics simulator- technical reference guide. Technical Report NIST IR 6467, National Institute of Standards and Technology, Gaithersburg, MD, 2000.
- [21] Frank McKenna, Gregory L. Fenves, and Michael H. Scott. OpenSees: A framework for earthquake engineering simulation. *Computing in Science & Engineering*, 13(4):58–66, 2011.
- [22] S. A. Mirza and J. G. MacGregor. Variations in dimensions of reinforced concrete members. *Journal of Structural Division, ASCE*, 105(ST4):751–766, 1979.
- [23] Zhuojun Nan, Mhd Anwar Orabi, Xinyan Huang, Yaqiang Jiang, and Asif Usmani. Structural-fire responses forecasting via modular AI. *Fire Safety Journal*, 140:103863, October 2023.
- [24] C. Perez, F. McKenna, and K. M. Mosalam. OpenSeesRT (version 0.0.63), 2024.
- [25] Michael Spearpoint. *Fire Engineering Design Guide*. Centre for Advanced Engineering, University of Canterbury, 2008.
- [26] Richard Sutton and Andrew Barto. *Reinforcement Learning: An Introduction*. MIT Press, 2018.
- [27] Guowei Zhang, Huaxiang Li, Guoqing Zhu, and Junyi Li. Temperature fields for fire resistance analysis of structures exposed to natural fires in large space buildings. *The Structural Design of Tall and Special Buildings*, 29(4):e1708, 2020.